

A Continuous Electrical Conductivity Model for Monolayer Graphene From Near Intrinsic to Far Extrinsic Region

Sitangshu Bhattacharya, *Member, IEEE*, Dipankar Saha, *Student Member, IEEE*, Aveek Bid, and Santanu Mahapatra, *Senior Member, IEEE*

Abstract—We present a closed-form continuous model for the electrical conductivity of a single layer graphene (SLG) sheet in the presence of short-range impurities, long-range screened impurities, and acoustic phonons. The validity of the model extends from very low doping levels (chemical potential close to the Dirac cone vertex) to very high doping levels. We demonstrate complete functional relations of the chemical potential, polarization function, and conductivity with respect to both doping level and temperature (T), which were otherwise developed for SLG sheet only in the very low and very high doping levels. The advantage of the continuous conductivity model reported in this paper lies in its simple form which depends only on three adjustable parameters: the short-range impurity density, the long-range screened impurity density, and temperature T . The proposed theoretical model was successfully used to correlate various experiments in the midtemperature and moderate density regimes.

Index Terms—Charged impurity, chemical potential, graphene, resistance, screening.

I. INTRODUCTION

IN RECENT years, graphene has demonstrated many exceptional transport properties not seen in conventional two dimensional (2D) systems. Of these the most puzzling is the dc electrical conductivity (σ). It is experimentally observed [1]–[4] that for the single-layer graphene (SLG) σ can show both insulating as well as metallic behavior in the same temperature range (regardless of the fact whether the SLG is suspended or on-substrate). What is more peculiar is that near the intrinsic zone (i.e., near the Dirac cone vertex)

Manuscript received April 11, 2014; revised September 5, 2014; accepted September 13, 2014. Date of publication October 1, 2014; date of current version October 20, 2014. The work is supported by the DST INSPIRE Faculty Grant-IFA 12 ENG-39, 2013, India. The review of this paper was arranged by Editor G. L. Snider.

S. Bhattacharya is with the Microelectronics Division, Department of Electronics and Communication Engineering, Indian Institute of Information Technology at Allahabad, Allahabad 211012, India (e-mail: sitangshu@iiita.ac.in).

D. Saha and S. Mahapatra are with the Nano-Scale Device Research Laboratory, Department of Electronic Systems Engineering, Indian Institute of Science, Bangalore 560012, India (e-mail: dipsah_etc@yahoo.co.in; santanu@cedt.iisc.ernet.in).

A. Bid is with the Mesoscopic Physics Group, Department of Physics, Indian Institute of Science, Bangalore 560012, India (e-mail: aveek.bid@physics.iisc.ernet.in).

Color versions of one or more of the figures in this paper are available online at <http://ieeexplore.ieee.org>.

Digital Object Identifier 10.1109/TED.2014.2358683

σ decreases with decreasing T ($\partial\sigma/\partial T > 0$), whereas in the extrinsic region σ decreases with increasing T ($\partial\sigma/\partial T < 0$). Further, a related question that has remained unanswered for quite some time is that because the electron–phonon deformation potential is quite small in SLG sheet, whether an ultraclean SLG (with dimensions in microns) should exhibit ballistic transport or not.

Whatever the case may be, these puzzling observations are now understood to arise mainly due to the interplay of three types of interactions, namely: 1) short-range impurity interactions; 2) long-range screened impurity interactions which appears while exfoliation of the graphene flakes (with the charged impurities located within the graphene sheet for suspended SLG or just beneath it for on-substrate SLG); and 3) temperature-induced acoustic electron–phonon interactions [4], [5]. By controlling the amount of charged impurities and the electron–phonon interaction strength (in other words, T) the entire behavior of σ can be reproduced theoretically [5]–[13]. However, these models are valid over a very restricted parameter space—they work either at $T = 0$ K [6], or in the regime very close to the Dirac cone vertex, or very far away from the vertex [5], [7], or is exhibited with complete numerical solutions [8]–[13]. This prevents one from understanding the variations in the midtemperature regime (near room temperature, where most devices work) and moderate carrier density regime. The reason for providing the solution in those extreme limits is mainly to bypass the analytical difficulties that occur while solving the Fermi–Dirac integral for arbitrary integrand cases. For example, in the limits $T \ll T_F$ and $T \gg T_F$ (where T_F is the Fermi temperature), one generally exploits the Sommerfeld’s expansion and the Maxwell’s statistics [14] to evaluate the asymptotic relation between the chemical potential and the Fermi energy. In fact, this has been used by Ando to exhibit the temperature dependence of the conductivity, as reported in [7]. Keeping this in mind, we were motivated to provide a seamless relation between the conductivity and the other parameters like temperature, charged impurities, and gate-induced carrier density. In this paper, we thus revisit the temperature-dependent charged impurity interaction in SLG through a novel continuous chemical potential model. We further use it to model the interband and intraband static polarization function considering Lindhard’s theory-based on

random phase approximation (RPA) [15], the Thomas–Fermi screening vector, the elastic scattering rate, and finally the Boltzmann-conductivity. The theoretical model formulated in this paper is advantageous considering its accuracy in describing the different measured dc conductivity values, and its simple form that depends only on the three parameters: temperature, short-range impurity densities and long-range impurity densities. The novelty of the proposed model lies in the following aspects.

- 1) Generally the chemical potential model for SLG is known only in the regions $T \ll T_F$ and $T \gg T_F$. Moreover, it suffers a discontinuity at $T = T_F$. Here we provide a continuous model of this chemical potential, that converges to the previously calculated values in the high T and low T limits without having any discontinuity at $T = T_F$.
- 2) To the best of our knowledge, the solution of the static dielectric function or, even the polarization function is asymptotically known only near the extreme limits $T \ll T_F$ and $T \gg T_F$. The proposed model estimates the aforesaid functions for all the temperatures.
- 3) Here we formulate a more general form of the Thomas Fermi screening wave vector which is valid for all temperatures. The long-range impurity scattering rate used in this paper is more generic one and the closed-form solution to this equation at all temperatures is obtained.

II. MODEL DEVELOPMENT

A. Graphene Chemical Potential Modeling

For an undoped, defect-less SLG sheet at absolute zero temperature the chemical potential (μ), which coincides with the Fermi energy (E_F), lies at the Dirac cone vertex. We start with the net carrier density

$$n_{2D} - p_{2D} = \frac{2}{\pi \gamma^2} (k_B T)^2 [F_1(\eta) - F_1(-\eta)] \quad (1)$$

in which n_{2D} and p_{2D} are the filled and empty states with energy $E > 0$ and $E < 0$ respectively, $\gamma = \hbar v_F$, $\hbar = h/2\pi$, h is the Planck's constant, v_F is the Fermi velocity, k_B is the Boltzmann's constant and $\eta = \mu(T)/k_B T$. The function $F_1(\eta)$ is the Fermi–Dirac integral of first order and is written as

$$F_1(\pm\eta) = \frac{1}{\Gamma(2)} \int_0^\infty \frac{x dx}{1 + e^{x \mp \eta}}. \quad (2)$$

Fig. 1(a) shows the numerical evaluation of the integral in (1) for all η and is compared with the functional form

$$F_1(\eta) - F_1(-\eta) \approx (2\ln 2)\eta + \frac{\eta^2}{2} \quad (3)$$

As the carriers density i.e., $n_{2D} - p_{2D}$ is conserved at all temperatures, evaluating (1) at $T = 0$ produces $n_{2D} - p_{2D} = (k_B T_F)^2 / \pi \gamma^2$ and equating this again to (1) at $T \neq 0$ by using (3) gives

$$\frac{1}{2} \left(\frac{T_F}{T} \right)^2 = \frac{(2\ln 2)\mu(T)}{k_B T} + \frac{1}{2} \left[\frac{\mu(T)}{k_B T} \right]^2 \quad (4)$$

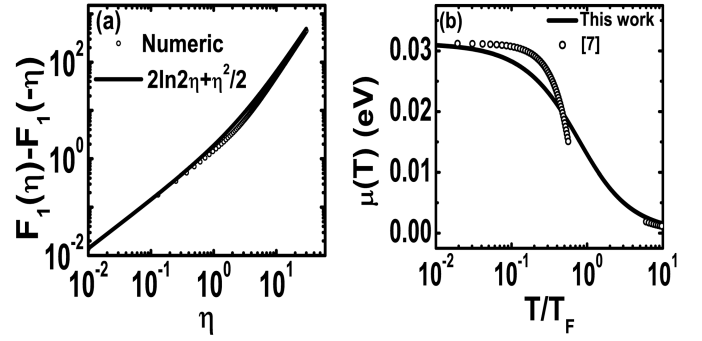


Fig. 1. (a) Variation of the Fermi–Dirac integral for all η using the numerically integrated value and the function $2\ln 2\eta + \eta^2/2$. (b) Chemical potential variation using the RHS function of (3) for all temperatures. The discontinuity at $T = T_F$ is clearly removed with good convergence. Here, $n_{2D} - p_{2D} = 7.2 \times 10^{14} \text{ m}^{-2}$, which gives E_F and T_F to be nearly 0.032 eV and 362 K respectively.

in which $E_F = k_B T_F$. From (4), $\mu(T)$ above the Dirac vertex can be written as

$$\mu(T) = 2\ln 2(k_B T) \left[-1 + \sqrt{1 + \left(\frac{T_F}{2\ln 2T} \right)^2} \right] \quad (5)$$

Thus, we see from (5) that $\mu(T)$ converges to E_F and 0 as $T/T_F \ll 1$ (high carrier density, $\eta \gg 1$) and $T/T_F \gg 1$ (low carrier density, $\eta \ll 1$) respectively. Equation (5) can also be compared with the analytic results given in [7] at the two extreme regimes as

$$\mu(T) \approx E_F \left(1 - \frac{\pi^2}{6} \left(\frac{T}{T_F} \right)^2 \right)$$

for $T/T_F \ll 1$ and $\mu(T) \approx (E_F/4\ln 2)(T_F/T)$ for $T/T_F \gg 1$. This is shown in Fig. 1(b) where we see the discontinuity at $T = T_F$ is removed when (5) is used. In Section II-B, we evaluate $\mu(T = 0)$ when additional charged impurities are present.

B. Graphene Fermi Energy Modeling

Evaluation of the Fermi energy at $T = 0$ K is still unresolved for ultraclean SLG sheet and is subject of percolation theory [16]. However, a statistical approach is followed to evaluate this near the vertex of the Dirac cone [16], where the Fermi energy corresponds to the induced carriers due to the gate potential (v_g) in the presence of screened charged impurities can be computed from [8]

$$n_{2D} - p_{2D} = \frac{1}{e} C_g [v_G - v_{\text{Dirac}}] \quad (6)$$

in which C_g is the gate capacitance, e is the electron charge, and v_{Dirac} is the Dirac potential that appears due to the charged impurities present either in the SLG sheet or just a few angstroms beneath it. In order to reduce the carrier density to zero, we see that v_G should at least equal v_{Dirac} . This value of v_G is called the cut-off or offset value. In the regime $v_G \ll v_{\text{Dirac}}$, the carriers respond to only v_{Dirac} as if there is a local potential applied, and provides the reason of obtaining a minimum conductivity. As the latter depends on the density

of the screened charged impurities, the minimum conductivity value is nonuniversal.

The potential near the Dirac cone vertex is evaluated about the region $\eta \ll 1$ where the charged impurities together with the charge fluctuations in the substrate create valleys (electrons) and hills (holes) of potentials of different heights. This in turn leads to carrier puddles [16] which have been also observed in experiments [17]. Hence, to obtain the exchange forces, the induced carrier density (n_d) due to the screened long-range charged impurities (which is a subject of ab initio study [18]) must be considered. The Dirac potential is then evaluated as $v_{\text{Dirac}} = -en_d/C_g$. In the following analyses, we assume that the charged scatterers are located very close to the SLG sheet (distance d) so that the correction factor (exponential part) in the Fourier transform of the 2D unscreened Coulomb potential function:

$$v(q) = \frac{2\pi e^2}{\kappa q} e^{-qd} \quad (7)$$

is small and slowly varying, thus could be relaxed for simplified solutions. Here κ is the effective substrate dielectric constant

$$\left(\frac{1}{2}(\kappa_{\text{substrate}} + \kappa_{\text{SLG}}) \right), \quad q = |\vec{k} - \vec{k}'| = 2k \sin\left(\frac{\theta_{kk'}}{2}\right)$$

is the Fourier space electron wave vector which is the change between initial (\vec{k}) and scattered vector (\vec{k}') and $\theta_{kk'}$ is the scattering angle. Further, as seen from [6], the induced feedback density $n_d \sim \sqrt{3}n_{\text{imp}}^2/4n_{\text{rms}}$, in which n_{imp} and n_{rms} are the screened long-range impurity and the root mean squared density of the disorder averaged density correlation function $(\langle \delta n \rangle^2)^{1/2}$ due to the fluctuating potentials resulting from puddles or spatial inhomogeneities. These fluctuations change the local chemical potential $(E_F^2)^{1/2}$ through the self-consistent residual density n^* which then feedback effectively to screen the density to n_d . Strictly speaking, the analytical model is still invalid in the zone of the large puddles (for $n_{\text{imp}} \ll 10^8 \text{ cm}^{-2}$) where the screening of the carriers are facilitated through the RPA and the Hubbard correction [19]. However, obtaining an ultraclean SLG sheet, where charged densities are $\leq 10^8 \text{ cm}^{-2}$, is an idealistic approach. For all practical purposes $n_{\text{imp}} \geq 10^8 \text{ cm}^{-2}$ and the effect of self-consistent n_d on n_{imp} and n_{rms} can be found out for SiO₂ or any other substrate as shown below.

The residual density results in $(\pi \gamma^2 n^*)^{1/2} = (E_F^2)^{1/2}$ which may be equated to the standard deviation of the fluctuating potential $(\overline{\Delta V^2})^{1/2} = ((V - \bar{V})^2)^{1/2}$ [16]. The second moment of the variance of the latter is

$$\overline{(V - \bar{V})^2} = \frac{n_{\text{imp}}}{2\pi} \int q dq |v_{\text{eff}}(q, T)|^2 \Big|_{T=0\text{K}} \quad (8)$$

in which $v_{\text{eff}}(q, T) = v(q)/\varepsilon(q, T)$ is the effective screened potential and is estimated from the Lindhard dielectric response function

$$\varepsilon(q, T) = 1 + \Pi(q, T)v(q) \quad (9)$$

where $\Pi(q, T)$ is the electric polarization function considering both inter and intraband carrier transitions. Under the static

condition and using compressibility sum rule at $T = 0 \text{ K}$ [15]

$$\Pi(q, T) = \int_{-\infty}^{\infty} \left(-\frac{\partial f}{\partial E} \right) N_{2D}(E) dE \quad (10)$$

becomes the density of states function $N_{2D}(k_F) = g_s g_v k_F / 2\pi \gamma$, where $g_s = g_v = 2$ are the spin and valley degeneracies. The use of (7) and (10) in (9) and (8) results

$$n^* = 2r_s^2 n_{\text{imp}} \left[\ln \left(1 + \frac{1}{2r_s} \right) - \frac{1}{1 + 2r_s} \right] \quad (11)$$

in which $r_s = e^2/\kappa \gamma$ is the density independent fine structure constant of graphene. Equation (11) is now evaluated for a known n_{imp} . This is then used in expression of n_d above to finally obtain v_{Dirac} for $n_{\text{rms}} \sim (3)^{1/2} n^*$ [6]. Once this Dirac potential is evaluated, the Fermi energy can finally be calculated from the expression $E_F = \gamma (\pi (n_{2D} - p_{2D}))^{1/2}$, in which the gate-induced net carrier density may now be easily evaluated from (6).

C. Static Polarization Function Modeling

The static polarization function following Lindhard's formulation can be written for graphene as [7]

$$\Pi(q, T) = -\frac{g_s g_v}{2L^2} \sum_{s, s', k} \frac{f_{sk} - f_{s'k'}}{E_{sk} - E_{s'k'}} (1 + s s' \cos \theta_{kk'}) \quad (12)$$

where L^2 denotes the system area, $s = \pm 1$ represents conduction (+1) and valance (-1) bands, $E_{sk} = s \gamma k$ is the band dispersion of electrons and holes, $\vec{k}' = \vec{k} + \vec{q}$ and

$$f_{sk} = \left[1 + \exp \left(\frac{E_{sk} - \mu}{k_B T} \right) \right]^{-1}$$

is the Fermi-function for the band index s . The form factor $1/2(1 + s s' \cos \theta_{kk'})$ occurs due to the graphene wave function chirality. Equation (12) is evaluated for all four combination of s , which corresponds to both intra and interband transition, and finally integrated over 2D k -space. Although cumbersome, (12) can be expanded as [5]

$$\begin{aligned} \frac{\Pi(q, T)}{N_{2D}(k_F)} &= \frac{\mu(T)}{E_F} + \frac{\pi q}{8k_F} + \frac{2T}{T_F} \ln \left(1 + e^{-\frac{\mu(T)}{k_B T}} \right) \\ &- \frac{1}{k_F} \int_0^{q/2} \sqrt{1 - \left(\frac{2k}{q} \right)^2} \left[\left(1 + e^{\frac{E+\mu(T)}{k_B T}} \right)^{-1} \right] dk \\ &- \frac{1}{k_F} \int_0^{q/2} \sqrt{1 - \left(\frac{2k}{q} \right)^2} \left[\left(1 + e^{\frac{E-\mu(T)}{k_B T}} \right)^{-1} \right] dk. \end{aligned} \quad (13)$$

At $T = 0 \text{ K}$, the Fermi function in the first integral goes to zero, while the second goes to 1 for $E < \mu$. The last integral then converges to the area of a unit radius circle in the first quadrant for $q \leq 2k$. This again gives $\Pi(q, 0) = N_{2D}(k_F)$. The $q \geq 2k$ zone shows Friedel oscillations of the spatial potential variation [14], whose effect on dc conductivity of SLG case has not yet been experimentally observed. As it can be seen, the analytical evaluation

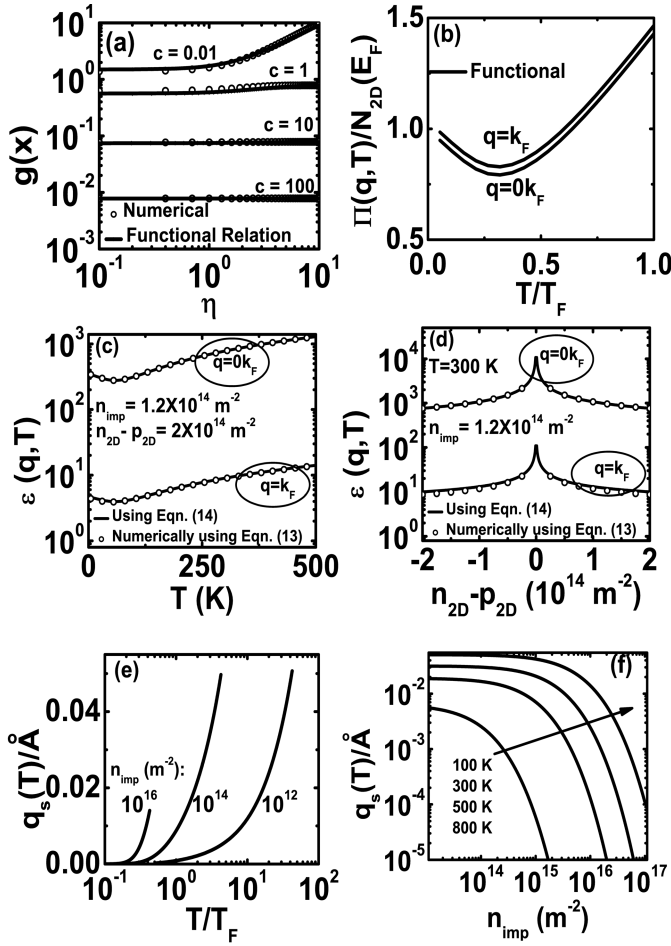


Fig. 2. (a) Variation of $g(x)$ with η for all values of T/T_F at $q \rightarrow 0$. (b) Polarization function variation with temperature T for $q = 0$ k_F and $q = k_F$ using the model (14). Higher values of q are neglected owing to the absence of back-scattering (Section II-D). Variation of $\epsilon(q, T)$ as function of (c) T and (d) carrier density. Symbols: numerical values from (13) in (9). Solid lines: from (14). (e) Variation of Thomas–Fermi screening vector [using (16)] with temperature in the region $q \rightarrow 0$ for different n_{imp} . (f) Variation of Thomas–Fermi screening vector [using (16)] with n_{imp} at different T .

of (13) for all T is difficult unless $T/T_F \ll 1$ or $T/T_F \gg 1$ approximations are used [5]. However, the dielectric function in (9) from (13) can be functionally represented over all temperatures as

$$\epsilon(q, T) = 1 + \frac{g_s g_v r_s E_F}{q \gamma} \left[\frac{\mu(T)}{E_F} + \frac{2T}{T_F} \ln(1 + e^{-\eta}) + \frac{\pi q}{8k_F} - \frac{T}{T_F} \left(\frac{\pi a}{\pi + 8a \frac{k_F T}{q}} \right) \right] \quad (14)$$

where $a = \ln[2(1 + \cosh(\eta))]$. Fig. 2(a) shows the numerical plot of the integral

$$g(x) = \int_0^{1/c} \sqrt{1 - (cx)^2} \left(\frac{1}{1 + e^{x+\eta}} + \frac{1}{1 + e^{x-\eta}} \right) dx$$

with the functional relation

$$\frac{\pi a}{\pi + 4ac} + \frac{\pi^2}{72(\ln 2)} \ln(1 + e^{-c})$$

in which $c = 2k_B T / \gamma q = (2k_F / q) T / T_F$. We thus see that for $q \rightarrow 0$ (long-wavelength approximation), $c \rightarrow \infty$, irrespective of the fact whether $T \ll T_F$ or $T \gg T_F$. This is shown in Fig. 2(b), considering the polarization function variation with temperature. To estimate the accuracy of our semianalytical model (14), we have further exhibited the variation of the dielectric function as functions of temperature and carrier density. This is done by evaluating the numerical integral (13) in (9) and comparing with (14), and is shown in Fig. 2(c) and (d), respectively. We see that our semianalytical model is in good agreement with the numerical one. At this point, it should be noted that the same variation of the polarization function with temperature is also exhibited elsewhere (which are obtained numerically in [20] and analytically at extreme temperature limits in [5]). Our model (14) may thus serve as an indirect way to confirm our accuracy. The effective 2D Coulomb screened potential under such conditions can then be written as

$$v_{\text{eff}}(q, T) = \frac{2\pi r_s \gamma}{q + q_s(T)} \quad (15)$$

in which

$$q_s(T) \sim \frac{g_s g_v r_s E_F}{\gamma} \left[\frac{\mu(T)}{E_F} + \frac{2T}{T_F} \ln \left(1 + \exp \left(-\frac{\mu(T)}{k_B T} \right) \right) \right] \quad (16)$$

is the Thomas–Fermi screening vector for all temperature. The variation of q_s with T as well as n_{imp} is shown in Fig. 2(e) and (f). We note that as $\mu(T)$ decreases with T , the increase of Thomas–Fermi vector is almost linear for high value of T/T_F or low value of η . The variation is, however, almost constant for low value of T/T_F or high value of η . Equations (15) and (16) are used to find the relaxation rates and consequently Boltzmann’s conductivity as shown in Section II-D.

D. Relaxation Rate and Boltzmann’s Conductivity

The elastic (intraband, with $ss' = +1$ only) scattering rate caused by charged impurities can be written as

$$\frac{1}{\tau_{\text{imp}}(E_k)} = \frac{2\pi n_{\text{imp}}}{\hbar} \int \frac{d^2 k'}{(2\pi)^2} |v_{\text{eff}}(q, T)|^2 \frac{(1 + \cos \theta_{kk'})}{2} \times (1 - \cos \theta_{kk'}) \delta(E_k - E_{k'}). \quad (17)$$

The form-factor $(1 + \cos \theta_{kk'})/2$ causes the scattering rate to vanish at both low angle (forward scattering, $\theta = 0$) as well as high angle (back-scattering, $\theta = \pi$). The use of (15) in (17) results in a scattering rate

$$\frac{1}{\tau_{\text{imp}}(E_k)} = \frac{8\pi^2 n_{\text{imp}} r_s^2 \gamma^2}{h E} \int_0^1 \frac{x^2 \sqrt{1 - x^2} dx}{[x f' + (\frac{q_s}{2k})]^2} \quad (18)$$

in which $f' = u - [v(T)/2kx + z(T)]$, $u = 1 + [\pi g_s g_v r_s / 8]$, $v(T) = (a g_s g_v / \gamma)(T/T_F) E_F$, and $z(T) = (8k_F a / \pi)(T/T_F)$. The integral in (18) can be analytically solved for $f' = 1$ [5]; however, complexity in evaluating Boltzmann conductivity integral will arise if the solution is not simple. The integral presented here is more general and can only be evaluated numerically. As shown in Fig. 3, we evaluate this integral

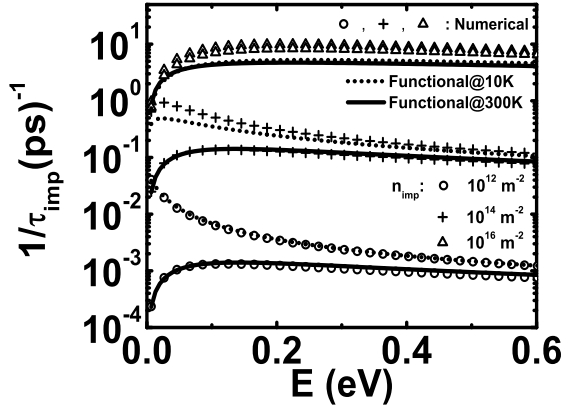


Fig. 3. Scattering rate variation due to charged screened impurities with energy. Symbols: numerical evaluation of (18). Solid and dotted lines: from (19). The carrier densities at $n_{\text{imp}} = 10^{12}$, 10^{14} , and 10^{16} m^{-2} are almost 1.9×10^{12} , 1.9×10^{14} , and 1.9×10^{16} m^{-2} , respectively.

numerically for all values of u , $v(T)$, $z(T)$, and $q_s(T)$, and compare the results with the functional form

$$\frac{1}{\tau_{\text{imp}}(E_k)} = \frac{2\pi^3 n_{\text{imp}} r_s^2 \gamma^2}{h} \frac{k^2}{E \left[u^2 k^2 + \left[\frac{\pi v(T)}{z(T)} \right]^2 k + [q_s(T)]^2 \right]}. \quad (19)$$

We find that the value of $1/\tau_{\text{imp}}(E_k)$ evaluated from (19) almost coincides with that obtained from (18) at all temperatures and n_{imp} . It should also be noted from the figure that for higher temperatures, the scattering rate is almost constant function of energy. Also at low temperatures when the impurity is made high, the scattering rate gradually changes its slope from negative to positive. In addition to charged impurity scattering, short range (e.g., due to missing carbon atoms, etc.) and acoustic phonon scattering is also involved whose rates are given as

$$\frac{1}{\tau_s(E_k)} = \frac{n_\delta V_\delta^2 v_F}{4\gamma^3} E \quad (20)$$

and

$$\frac{1}{\tau_{\text{ac}}(E_k)} = \frac{D_A^2 k_B T}{4\hbar^3 \rho_m v_F^2 v_s^2} E \quad (21)$$

in which a δ -type potential is assumed with strength V_δ and density n_δ for short-range scattering. Here $D_A = 19$ eV, $\rho_m = 7.6 \times 10^{-7}$ kgm^{-2} and $v_s = 2.1 \times 10^4$ ms^{-1} are the elastic acoustic deformation potential constant, mass density, and longitudinal phonon velocity respectively.

Equations (19), (20), and (21) can be combined through the Matthiessen's rule

$$\frac{1}{\tau(E_k)} = \frac{1}{\tau_{\text{imp}}(E_k)} + \frac{1}{\tau_s(E_k)} + \frac{1}{\tau_{\text{ac}}(E_k)} \quad (22)$$

to provide Boltzmann electrical conductivity as

$$\sigma = \frac{e^2 v_F^2}{2} \int N_{2D}(E) \tau(E) \left(-\frac{\partial f(E)}{\partial E} \right) dE. \quad (23)$$

Resolving the slope $(-\partial f(E)/\partial E)$ into secant hyperbolic function (23) can be rewritten as

$$\sigma = \frac{e^2}{\pi^2 \hbar r_s^2 n_{\text{imp}}} \int_{-\frac{\eta}{2}}^{\infty} \left[\frac{Ax^2 + Bx + C}{1 + \Xi(Ax^2 + Bx + C)} \right] \text{sech}^2 x dx \quad (24)$$

in which

$$A(T) = 4 \left(\frac{u k_B T}{\gamma} \right)^2$$

$$B(T) = 4 \left(\frac{u k_B T}{\gamma} \right)^2 \eta + \frac{2[\pi v(T)]^2}{\gamma z(T)} k_B T$$

$$C(T) = \left(\frac{\eta u k_B T}{\gamma} \right)^2 + \frac{[\pi v(T)]^2}{\gamma z(T)} k_B T \eta + [q_s(T)]^2$$

and

$$\Xi(T) = \frac{h}{2\pi n_{\text{imp}} r_s^2} \left[\frac{n_\delta V_\delta^2 v_F}{4\gamma^3} + \frac{D_A^2 k_B T}{4\hbar^3 \rho_m v_F^2 v_s^2} \right].$$

An approximated closed-form expression of (24) could be given as (for all η and impurities)

$$\sigma = \frac{e^2}{\pi^2 \hbar r_s^2 n_{\text{imp}}} \left(\frac{\pi^4 \ln 2}{28} \right) C(T) \times \left[1 + \frac{\pi^2}{7} C(T) \Xi(T) + \frac{\pi^2}{72} \Xi(T) \{A(T) + B(T) + C(T)\} \right]^{-1}. \quad (25)$$

III. RESULTS AND DISCUSSION

Fig. 4(a) shows the comparison of the results of numerical integration in (24) with our rigorous result (25) for all n_{imp} and the short-range scattering potential $n_\delta V_\delta^2$. We see that (25) follows (24) quite well from low $n_\delta V_\delta^2$ [1.5 (eV \AA^2)] to a high $n_\delta V_\delta^2$ [15 (eV \AA^2)] as shown in Fig. 4(a) and (b), respectively. The carrier density shown in both Fig. 4(a) and (b) are 1.9×10^{12} m^{-2} , 1.9×10^{14} m^{-2} , and 1.9×10^{16} m^{-2} for $n_{\text{imp}} = 10^{12}$ m^{-2} , 10^{14} m^{-2} , and 10^{16} m^{-2} , respectively. The slight mismatch between σ for higher n_{imp} [Fig. 4(b)] is seen because of the enlarged scale and can be neglected, where we note that the nature of variations are preserved. The reason for the slight mismatch of our semianalytical model (25) with the numerical (24) is the absence of its closed-form solution. Evaluation of the solution of (24) is an involved task unless special approximation is done. Our model (25) suggests that the disparity may become larger for very high short-range impurities [in the range large than 10 (eV \AA^2)]. However, this corresponds to a sample with lot of missing carbon atoms. It should be noted that the main objective of this paper is certainly not to match the data closely point-by-point, but rather to provide a quick variation estimation and thumb rule to guess the SLG electrical conductivity.

A number of interesting observations regarding the temperature dependence of σ ($\partial\sigma/\partial T$) can be made by comparing Fig. 4(a) and (b) in the absence of any gate voltage (minimum conductance condition at $T = 0$ K). For low-density of short-range impurities we observe the following

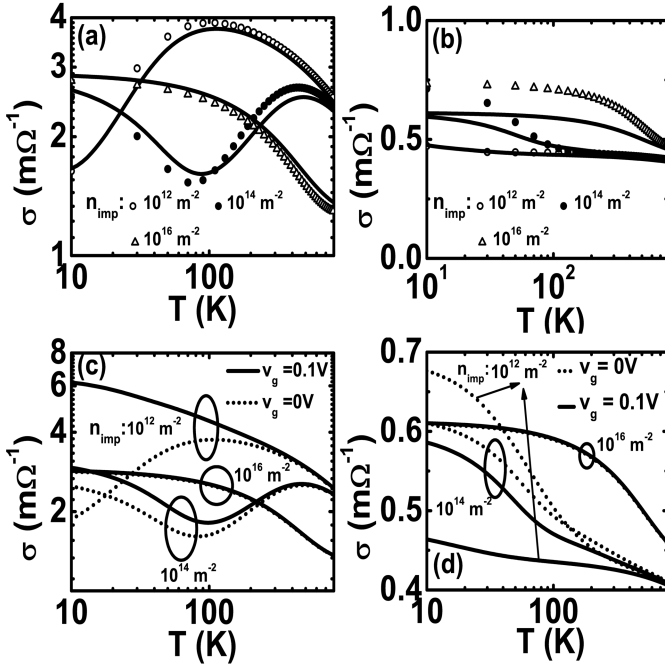


Fig. 4. (a) Conductivity variation with temperature for different n_{imp} at $v_g = 0$ V and $n_\delta V_\delta^2 = 1.5$ ($\text{eV}\ \text{\AA}^2$). Symbols: numerical evaluation of (24). Solid lines: from (25). (b) All cases of (a) at $n_\delta V_\delta^2 = 15$ ($\text{eV}\ \text{\AA}^2$). (c) All cases of (a) at two different gate voltages $v_g = 0$ and 0.1 V. (d) All cases of (b) at two different gate voltages $v_g = 0$ and 0.1 V. In (c) and (d), the solid lines and the symbols are generated from (25) at two different v_g .

behavior of σ with increasing temperature: 1) at low n_{imp} the temperature dependence of σ changes from nonmetallic to metallic; 2) near moderate n_{imp} ($\sim 10^{14}$ m^{-2}) the transformation is completely opposite; 3) for high n_{imp} ($\sim 10^{16}$ m^{-2}), σ exhibits a pure metallic (slow, below room temperature while high, above room temperature) variation; 4) cross-over regions are exhibited for increasing n_{imp} . For large short-range impurities as the temperature is increased above $T = 0$ K; 5) we lose all nonmetallic-type behavior, 6) for low n_{imp} , σ always exhibits slow metallic variation for all temperatures; and 7) magnitude of σ is always proportional to n_{imp} . In case of $v_g \gg v_{\text{Dirac}}$ [i.e., low n_{imp} , Fig. 4(c)], a metallic behavior is observed at low temperatures as was seen for high n_{imp} . As v_{Dirac} begins to exceed v_g , the behavior is always metallic. When the short-range potential is high [Fig. 4(d)] with $v_g \ll v_{\text{Dirac}}$, again a metallic behavior is observed. The carrier densities in these two figures are the similar to that shown in Fig. 4(a) and (b).

The temperature dependence of σ due to long-range screened impurity interactions, short-range impurity interactions, and acoustic phonons for $n_{\text{imp}} = 10^{14}$ m^{-2} and $n_\delta V_\delta^2 = 1.5$ ($\text{eV}\ \text{\AA}^2$) is shown in Fig. 5. Although the results are known using numerical techniques [5], [20], we establish this with our single semianalytical model over the entire range of T/T_F . We see that near the Dirac cone vertex, the conductivity is always dominated by the acoustic phonons, which makes SLG transport as diffusive at all temperature. In the absence of long-range impurities and acoustic phonons, σ is constant with temperature due to

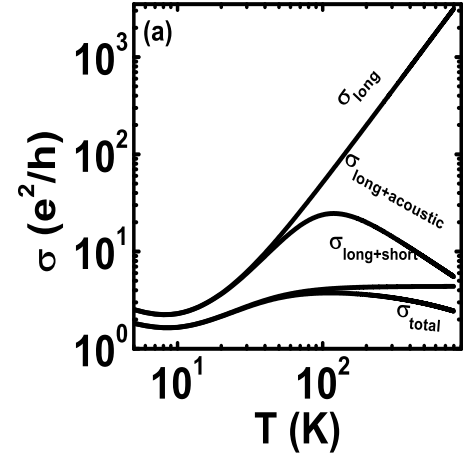


Fig. 5. Conductivity variation with temperature from (25), demonstrating the effect of different scattering strength.

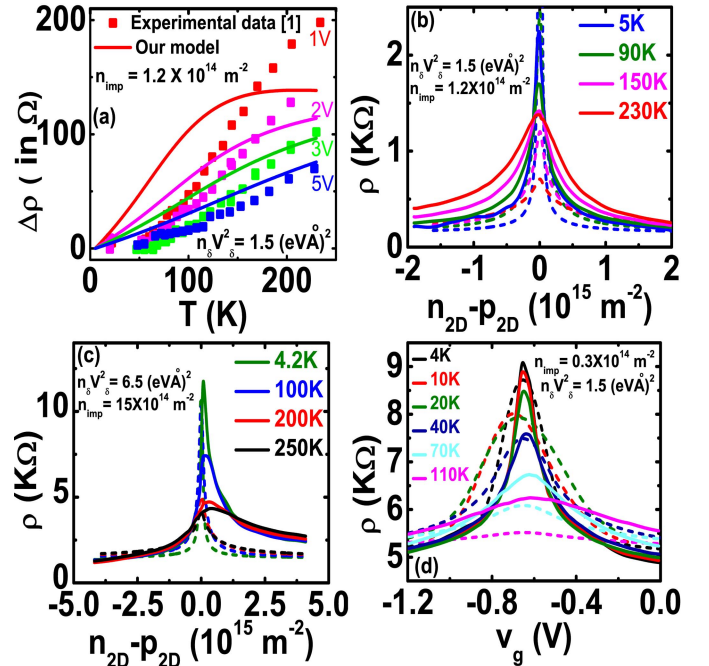


Fig. 6. Reproduction of the experimental data of conductivity from (a) Bolotin *et al.* [1] [symbols are the data and solid lines are our semianalytical model from (25)], (b) Bolotin *et al.* [1] [solid lines are the data and dotted lines are from (25)], (c) Du *et al.* [2] [solid lines are the data and dotted lines are from (25)], and (d) Mayorov *et al.* [3] [solid lines are the data and dotted lines are from (25)].

constant scattering rate. Intrinsic SLG thus behaves as metal ($\partial\sigma/\partial T > 0$) at high temperatures and has a nonmetallic behavior ($\partial\sigma/\partial T < 0$) in lower temperature region. Fig. 6(a)–(d) shows the variation of σ with temperature and induced charge density and showcases the regeneration of the data (which also been presented in [20] numerically) obtained from three recent experiments, and stands as the validation of our semianalytical model. Fig. 6(a) and (b) shows the data from Bolotin *et al.* [1], where the measurement was done on suspended SLG sheet in the temperature range 5–230 K. The figure is regenerated from the off-set voltage $v_g = -v_{\text{Dirac}}$.

As also suggested by [20], from our relation we observe that the best fit is obtained for $n_{\text{imp}} = 1.2 \times 10^{10} \text{ cm}^{-2}$ and $n_{\delta}V_{\delta}^2 = 1.5 \text{ (eV \AA)}^2$. The crossing over of the curves suggests that near the Dirac cone vertex, SLG behaves like a nonmetal. Fig. 6(c) shows the correlation of our model with the data of Du *et al.* [2] in the temperature range 4.2–250 K. In this case, the best fit is for $n_{\text{imp}} = 6.5 \times 10^{10} \text{ cm}^{-2}$ and $n_{\delta}V_{\delta}^2 = 15 \text{ (eV \AA)}^2$, which was also previously arrested in [20]. Fig. 6(d) shows our model validation with Mayorov *et al.* [3] in the temperature range 4–110 K where the device resistance of 4.5 K Ω is added to the SLG sheet resistance together with the offset voltage of about 0.65 V. In all cases, the device capacitances (mostly classical) were kept same in our calculations as evident from the reported device geometries.

In all our calculations, we did not include contribution to the conductivity from flexural phonons which appears for films that are relaxed with only the ends clamped by contacts. In this case, the contribution will come from $q \geq 2k$ part [21], and our models can be reformulated to include this contribution. The mobility and mean-free path lengths can be deduced from (25) subject to a careful estimation between the induced carrier density and the Dirac cone vertex density. We have not considered the interaction picture due to resonant scatterings which mimics inclusions of hydrocarbons, lattice defects like vacancies [22], which, however, may arise depending on the type of synthesis of graphene flakes and is beyond the scope of this manuscript. Additionally, the quasi-elastic acoustic phonon-scattering interaction picture is assumed here by considering the carrier density such that the Bloch-Grüniesen temperature is less than T [23], [24]. Apart from this, we have considered the acoustic deformation potential constant to be 19 eV [23] whose accuracy is yet to be determined [24]. The theoretical models derived in this paper can be used as a rule of thumb for a faster and compact prediction of SLG conductivity over all temperatures and gate-induced densities ($\geq 10^{12} \text{ m}^{-2}$) to understand the behavior of SLG-based transistors at the scaling limits.

IV. CONCLUSION

We propose a physics-based closed-form electrical conductivity model for monolayer graphene, which is continuous from near intrinsic to far extrinsic regime. We consider the combined effects of short-range impurities, long-range screened impurities, and the acoustic phonon to develop the model. The proposed model depends only on three adjustable parameters: the short-range impurity density, the long-range screened impurity density, and the temperature. An estimation of the impurity density in the SLG samples can be done through our model (25) which yields good agreement with the experimental results.

REFERENCES

- [1] K. I. Bolotin, K. J. Sikes, J. Hone, H. L. Stormer, and P. Kim, "Temperature-dependent transport in suspended graphene," *Phys. Rev. Lett.*, vol. 101, no. 9, pp. 096802-1–096802-4, 2008.
- [2] X. Du, I. Skachko, A. Barker, and E. Y. Andrei, "Approaching ballistic transport in suspended graphene," *Nature Nanotechnol.*, vol. 3, pp. 491–495, Jul. 2008.
- [3] A. S. Mayorov *et al.*, "How close can one approach the Dirac point in graphene experimentally?" *Nano Lett.*, vol. 12, no. 9, pp. 4629–4634, 2012.
- [4] J.-H. Chen, C. Jang, S. Adam, M. S. Fuhrer, E. D. Williams, and M. Ishigami, "Charged-impurity scattering in graphene," *Nature Phys.*, vol. 4, pp. 377–381, Apr. 2008.
- [5] E. H. Hwang and S. D. Sarma, "Screening-induced temperature-dependent transport in two-dimensional graphene," *Phys. Rev. B*, vol. 79, no. 16, pp. 165404-1–165404-12, 2009.
- [6] S. Adam, E. H. Hwang, V. M. Galitski, and S. D. Sarma, "A self-consistent theory for graphene transport," *Proc. Nat. Acad. Sci. United States Amer.*, vol. 104, no. 47, pp. 18392–18397, 2007.
- [7] T. Ando, "Screening effect and impurity scattering in monolayer graphene," *J. Phys. Soc. Jpn.*, vol. 75, no. 7, pp. 074716-1–074716-7, 2006.
- [8] J. Fernández-Rossier, J. J. Palacios, and L. Brey, "Electronic structure of gated graphene and graphene ribbons," *Phys. Rev. B*, vol. 75, no. 20, pp. 205441-1–205441-8, 2007.
- [9] K. Nomura and A. H. MacDonald, "Quantum transport of massless Dirac fermions," *Phys. Rev. Lett.*, vol. 98, no. 7, pp. 076602-1–076602-4, 2007.
- [10] V. V. Cheianov and V. I. Fal'ko, "Friedel oscillations, impurity scattering, and temperature dependence of resistivity in graphene," *Phys. Rev. Lett.*, vol. 96, no. 22, pp. 226801-1–226801-4, 2006.
- [11] M. Trushin and J. Schliemann, "Minimum electrical and thermal conductivity of graphene: A quasiclassical approach," *Phys. Rev. Lett.*, vol. 99, no. 21, pp. 216602-1–216602-4, 2007.
- [12] X.-Z. Yan, Y. Romiah, and C. S. Ting, "Electric transport theory of Dirac fermions in graphene," *Phys. Rev. Lett.*, vol. 77, no. 12, pp. 125409-1–125409-4, 2008.
- [13] L. Liu, Y. Lu, and J. Guo, "Coupled electro-thermal simulation for self-heating effects in graphene transistors," *IEEE Trans. Electron. Devices*, vol. 60, no. 8, pp. 2598–2603, Aug. 2013.
- [14] J. M. Ziman, *Theory of Solids*, 2nd ed. Cambridge, U.K.: Cambridge Univ. Press, 1972.
- [15] G. D. Mahan, *Many-Particle Physics*, 2nd ed. New York, NY, USA: Springer-Verlag, 1990.
- [16] V. M. Galitski, S. Adam, and S. D. Sarma, "Statistics of random voltage fluctuations and the low-density residual conductivity of graphene," *Phys. Rev. B*, vol. 76, no. 24, pp. 245405-1–245405-7, 2009.
- [17] J. Martín *et al.*, "The nature of localization in graphene under quantum Hall conditions," *Nature Phys.*, vol. 5, pp. 669–674, Jul. 2009.
- [18] E. Rossi and S. D. Sarma, "Ground state of graphene in the presence of random charged impurities," *Phys. Rev. Lett.*, vol. 101, no. 16, pp. 166803-1–166803-4, 2008.
- [19] M. Jonson, "Electron correlations in inversion layers," *J. Phys. C, Solid State Phys.*, vol. 9, no. 16, pp. 3055–3071, 1976.
- [20] S. D. Sarma and E. H. Hwang, "Density-dependent electrical conductivity in suspended graphene: Approaching the Dirac point in transport," *Phys. Rev. B*, vol. 87, no. 3, pp. 035415-1–035415-15, 2013.
- [21] H. Ochoa, E. V. Castro, M. I. Katsnelson, and F. Guinea, "Scattering by flexural phonons in suspended graphene under back gate induced strain," *Phys. E*, vol. 44, no. 6, pp. 963–966, 2012.
- [22] A. Ferreira, J. Viana-Gomes, J. Nilsson, E. R. Mucciolo, N. M. R. Peres, and A. H. Castro Neto, "Unified description of the dc conductivity of monolayer and bilayer graphene at finite densities based on resonant scatterers," *Phys. Rev. B*, vol. 83, pp. 165402-1–165402-22, 2011.
- [23] E. H. Hwang and S. D. Sarma, "Acoustic phonon scattering limited carrier mobility in two-dimensional extrinsic graphene," *Phys. Rev. B*, vol. 77, no. 11, pp. 115449-1–115449-6, 2008.
- [24] H. Ochoa, E. V. Castro, M. I. Katsnelson, and F. Guinea, "Temperature-dependent resistivity in bilayer graphene due to flexural phonons," *Phys. Rev. B*, vol. 83, no. 23, pp. 235416-1–235416-15, 2011.



Sitangshu Bhattacharya (M'13) received the Ph.D. degree from Jadavpur University, Kolkata, India, in 2009.

He is currently an Assistant Professor with the Indian Institute of Information Technology at Allahabad, Allahabad, India. His current research interests include many body physics and Boltzmann transport in transparent sheets.



Dipankar Saha (S'12) received the M.Tech. degree from Jadavpur University, Kolkata, India, in 2013. He is currently pursuing the Ph.D. degree with the Nano Scale Device Research Laboratory, Department of Electronic Systems Engineering, Indian Institute of Science, Bangalore, India.

His current research interests include electro-thermal transport in nanoelectronic devices and modeling and simulation of nanoscaled devices with 2-D channel materials.



Santanu Mahapatra (M'08–SM'10) received the Ph.D. degree from the École Polytechnique Fédérale de Lausanne, Lausanne, Switzerland, in 2005.

He is currently an Associate Professor with the Indian Institute of Science, Bangalore, India.

Prof. Mahapatra was a recipient of the Ramanna Fellowship from the Department of Science and Technology, Government of India, for his contribution in compact modeling, in 2012.



Aveek Bid received the Ph.D. degree from the Department of Physics, Indian Institute of Science (IISc), Bangalore, India, in 2006.

He is currently an Assistant Professor with the Department of Physics, IISc. His current research interests include transport properties of mesoscopic devices.